

Second-harmonic imaging microscopy for time-resolved investigations of transition metal dichalcogenides

J. E. Zimmermann,¹ B. Li,² J. Hone,² U. Höfer,¹ and G. Mette^{1, a)}

¹⁾*Fachbereich Physik und Zentrum für Materialwissenschaften, Philipps-Universität, 35032 Marburg, Germany*

²⁾*Department of Mechanical Engineering, Columbia University, New York 10027, United States*

(Dated: 20 April 2020)

Two-dimensional transition metal dichalcogenides (TMDC) have shown promise for various applications in optoelectronics and so-called valleytronics. Their operation and performance strongly depend on the stacking of individual layers. Here, optical second-harmonic generation (SHG) in imaging mode is shown to be a versatile tool for systematic time-resolved investigations of TMDC monolayers and heterostructures in consideration of the material's structure. Large sample areas can be probed without the need of any mapping or scanning. By means of polarization dependent measurements, the crystalline orientation of monolayers or the stacking angles of heterostructures can be evaluated for the whole field of view. Pump-probe experiments then allow to correlate observed transient changes of the second-harmonic response with the underlying structure. The corresponding time-resolution is virtually limited by the pulse duration of the used laser. As an example, polarization dependent and time-resolved measurements on mono- and multilayer MoS₂ flakes grown on a SiO₂ / Si(001) substrate are presented.

^{a)}gerson.mette@physik.uni-marburg.de

I. INTRODUCTION

Two-dimensional (2D) materials have been intensively investigated since the first successful isolation of graphene¹ and this interest has been stimulated further by the discovery of the special properties of single-layer transition metal dichalcogenides (TMDC)^{2,3}. Van-der-Waals coupled 2D materials now span the whole range from metallic over semiconducting up to isolating materials and their combination leads to fascinating opportunities for designing stacked heterostructures^{4,5}. Heterostructures of TMDCs have shown promise for various optoelectronic applications (cf.⁶ and refs. therein). Moreover, future applications beyond conventional optoelectronics might be based on the coupled spin and valley physics of TMDC monolayers due to their broken inversion symmetry⁷. This coupling allows the excitation of specific spin carriers into a particular valley which has been demonstrated by optical pumping with circularly polarized light^{8–10}. These findings pave the way for a new class of prospective devices called valleytronics.

TMDC monolayer and heterostructure samples available at the moment are typically smaller than $(100\,\mu\text{m})^2$. Furthermore, they usually exhibit considerable spatial inhomogeneity due to intrinsic defects within the layers or extrinsic inhomogeneity such as substrate roughness, interlayer bubbles or impurities. Therefore, it is particularly important to utilize appropriate imaging techniques for their exploration. The energy alignment of TMDC heterostructures^{11–15} as well as interlayer charge- and energy-transfer processes^{16–23} are of particular interest in fundamental and applied research. Due to the Van-der-Waals coupling, arbitrary layer stacking is possible. Rotational misfit between two TMDC monolayers of a layered structure results in a corresponding rotation of the hexagonal Brillouin zones of the two layers leading to momentum-mismatched interlayer excitations. Therefore, the stacking influences charge and energy transfer and thereby the performance of the device. It has been shown that the interlayer coupling of homo-stacked layers depends considerably on the respective stacking angles^{24–27} and the same should hold for the coupling of hetero-bilayers^{28–30}. Indeed, a distinct difference in the exciton recombination of coherently and randomly stacked MoS₂/WS₂ heterostructures was observed³¹. Furthermore, a strong influence of the stacking angle on the formation dynamics of interlayer excitons has been reported recently for WSe₂/WS₂²³.

Thus, systematic studies are highly needed to investigate how structural characteristics like the stacking angle of 2D heterostructures correlate with other physical properties of the materials such as the existence and dynamics of charge transfer excitons. In this work, we demonstrate that

spatially resolved optical second-harmonic generation (SHG), i.e. SHG imaging microscopy, is a powerful experimental technique to perform time-resolved studies in consideration of the material's structure. It allows studying systematically both the orientation and the charge carrier dynamics of TMDC monolayers and heterostructures with the same experimental setup. In particular, a complementary technique to analyze the stacking of the material is not needed. As an example, we report time-resolved SHG imaging microscopy studies on MoS₂ mono- and multi-layer flakes grown by chemical vapor deposition (CVD) on a 285 nm SiO₂/Si(001) substrate.

II. TIME-RESOLVED SHG ON TMDCS

Previous studies already demonstrated that second-harmonic generation is a versatile technique to investigate single- and multilayers of TMDCs^{32–44}. It has been shown that the SH response of the TMDCs exhibits a dramatic odd-even oscillation with the number of layers consistent with the absence (presence) of inversion symmetry in odd (even) layers^{32–35}. Rotational anisotropy SHG measurements probing the SH response of TMDC monolayers as a function of the crystal orientation reveal the expected three-fold rotational symmetry^{33–37}. This allows the determination of crystallographic orientations for single-layer flakes^{33–37}, domain boundaries and orientations of CVD grown monolayer structures^{35,38,39} as well as stacking angles of twisted bilayers⁴⁰.

While all these examples represent basically static SH experiments for structural characterization of TMDC materials, time-resolved SHG has been applied in particular to study the dynamics of various phenomena at surfaces and interfaces of bulk semiconductors. Its sensitivity to symmetry changes and to interface electronic states has been exploited for time-domain investigations of phase transformations^{45,46}, of adsorbate reactions⁴⁷, of interface-specific electron dynamics^{48–50} and to detect transient electric fields at interfaces^{51–53}. Those time-resolved experiments on TMDC samples have to cope with the small flake/domain size of exfoliated and CVD grown samples available at the moment. Therefore, almost all previous linear and nonlinear optical experiments were performed at normal incidence by means of microscope objectives ($\times 100$) with short working distances and probe beams focused to spot diameter of $\approx 1 \mu\text{m}$. This kind of setup is disadvantageous for time-resolved pump-probe studies like SHG because it makes the non-collinear incidence of pump and probe beam difficult. As the pump beam also generates SH signal, this has to be differentiated from the SH response of the probe beam. Furthermore, the time-resolution is limited due to dispersion of the used optical elements. These difficulties might explain why, to the best of our

knowledge, there is only one published time-resolved SHG study on TMDCs. Here, the dynamical SH response of single-layer MoS₂ to intense above-bandgap photo-excitation was investigated⁴¹.

SHG imaging microscopy combines the advantages of time-resolved SHG with an optical microscopy setup. The SH response of the sample is imaged optically magnified on a CCD chip. Similar setups have been used to study surface reactions like desorption or diffusion^{54–56} as well as electric field distributions and carrier motion^{57–60}. SHG imaging microscopy copes with both of the discussed challenges of time-resolved studies on TMDCs. On the one hand, the SH response of pump and probe beam can be separated very easily. On the other hand, the time-resolution is virtually limited by the pulse duration of the laser system. The SH response of large sample areas ($\approx 400 \times 400 \mu\text{m}^2$) can be probed without the need of any mapping or scanning. By means of polarization dependent measurements, the crystalline orientation of single-layer flakes and domains, or the stacking angles of heterostructures can be evaluated for the whole field of view. Pump-probe experiments at the corresponding area then allow to correlate observed transient changes of the SH response with the underlying structure. With this technique polarization- and time-resolved measurements can be performed systematically and routinely. SHG imaging microscopy is also suited to study fluence dependent phenomena⁵⁶.

III. EXPERIMENTAL PROCEDURE

The experiments were performed under ambient conditions using 50 fs laser pulses generated by a femtosecond Ti:Sapphire laser amplifier system (Coherent RegA) operating at 800 nm with a repetition rate of 150 kHz. The main part of the amplifier output (90 %) is used to pump a travelling-wave optical parametric amplifier (OPA) operating in the visible range. The output of the OPA is compressed by a pair of LaFN28 Brewster prisms. This visible pump beam is then focussed under the angle of 50° onto the sample as illustrated in Fig.1. The remaining part of the amplifier output (10 %) is focused on the sample under an angle of 18° to probe the SH response. Due to the different incident angles the SH signals generated by the pump and the probe beam are spatially separated.

The specular reflected SH response of the probe beam is imaged optically magnified by a camera lens (NIKON NIKKOR, 1 : 1.4 ED, $f = 50\text{mm}$) on an electron-multiplied CCD chip (PRINCETON INSTRUMENTS ProEM-HS) with a size of 1024×1024 pixels; each pixel covers an area of $13 \times 13 \mu\text{m}^2$ on the chip. The camera is sensitive in a spectral range from 300 nm up

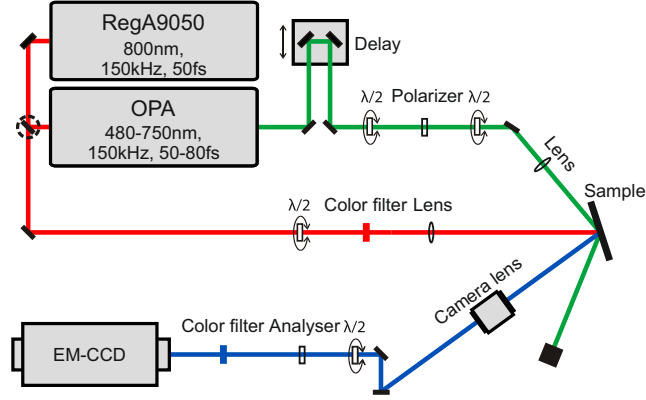


FIG. 1. (Color online) Experimental setup: fs-laser pulses are generated by a Ti:Sapphire laser amplifier system (RegA). The main part of the amplifier output (90 %) is used to pump an optical parametric amplifier (OPA) generating visible pump pulses. The remaining part of the amplifier output is used to probe the SH response. Pump and probe beam are focussed onto the sample under an angle of 50° and 18° , respectively. The specular reflected SH light of the probe pulse is imaged optically magnified by a camera lens on the CCD camera.

to 1050nm and was operated in full image mode. The used magnification was $M \approx 35 - 40$, thus the visible sample region on the CCD was about $400 \times 400 \mu\text{m}^2$. The overall resolution of our imaging microscopy setup is better than $4 \mu\text{m}$ as determined by a standard resolution target (c.f. Fig. S1 in the supplementary material). Thus, the resolution is close to the diffraction limit of $\approx 2 \mu\text{m}$.

The time-delay between pump and probe beam is varied by a motorized delay stage. The polarization of pump and probe beam can be varied by means of $\lambda/2$ -plates. The polarization of the second-harmonic (SH) response is analyzed by a combination of a $\lambda/2$ -plate and analyzer. Color filters for separation of both the incident ω - and detected 2ω -light have been used (RG715, FBH400-40). The spot diameter of pump and probe beam on the sample [full width at half maximum (FWHM)] were $160 \mu\text{m}$ and $200 \mu\text{m}$, respectively. A combination of $\lambda/2$ -plate and polarizer enable the continuous variation of the incident pump fluences on the sample. The incident fluence of the 600-nm pump beam was $\approx 55 \mu\text{J}/\text{cm}^2$ and $\approx 190 \mu\text{J}/\text{cm}^2$ for the 800-nm probe beam. Long term measurements with these fluences applied did not exhibit any multishot damage.

The studied TMDC sample consists of mono- and multilayers of MoS_2 flakes which were CVD grown on a 285 nm $\text{SiO}_2/\text{Si}(001)$ substrate⁶¹. Photoluminescence (PL) measurements of

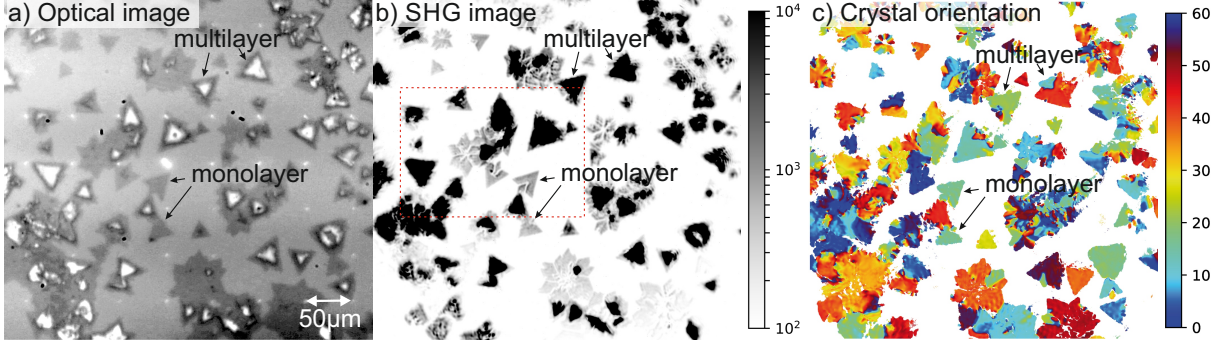


FIG. 2. a) Optical image of the CVD grown MoS₂ sample in comparison with b) the respective intensity-inverted SH microscopy image ($400 \times 400 \mu\text{m}^2$). The MoS₂ mono- and multilayers are identified as triangular flakes (some marked by arrows). The multilayers exhibit an one order of magnitude stronger SH response than the monolayers. The red box marks the region used for the polarization- and time-dependent evaluations shown in Figs. 3 and 4. c) Crystal angle modulo 60° for each individual pixel evaluated from polarization-dependent measurements. Different crystalline domains can be easily identified.

the monolayer flakes shown in Fig. S2 of the supplementary material exhibit an intense PL peak centered around 1.85 eV indicating low doping during the CVD process and relative low defect density compared to exfoliated MoS₂. Fig. 2 a) and b) show an optical microscope image ($\times 50$) in comparison to the respective SHG microscopy image (P-polarized SH component, $t_{\text{exposure}} = 300 \text{ s}$) which is intensity-inverted for better comparability. Using a logarithmic color scale, one can differentiate easily between the triangular shaped mono- and multilayer crystals. Monolayers appear in gray color on the bright SiO₂ /Si(001) substrate, while the multilayer flakes appear black. They exhibit an up to a factor of 30 times stronger SH response than the monolayer. This is in contrast to the reported negligible SH signals from MoS₂ bulk material³³ which naturally occurs in the inversion symmetric AA' (2H) stacking. This discrepancy can be explained by an AB (3R) layer stacking which was calculated to have very similar adsorption energy in multilayer growth⁶². Thus, depending on the exact growth conditions, multilayers can grow predominantly AB stacked with the top layer zero degree aligned with the bottom layer²⁴. The resulting multilayer structures are primarily non-centrosymmetric and the higher SH intensity can therefore be explained by a constructive interference of the stacked monolayer SH signals.

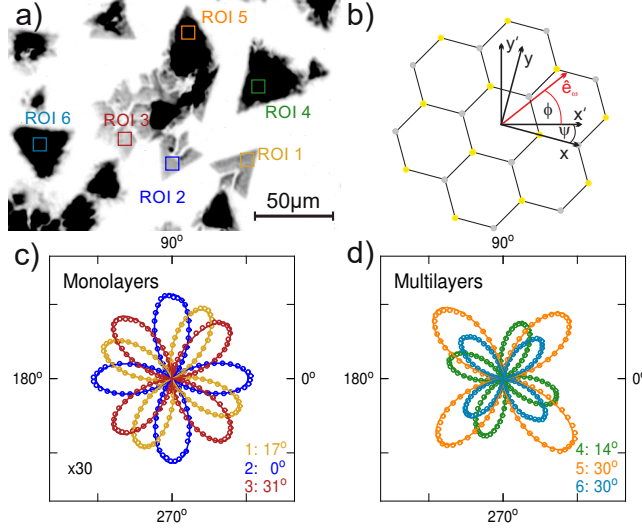


FIG. 3. (a) SHG microscopy image (P-polarized SH component, $t_{\text{exposure}} = 60\text{s}$) with colored regions of interests of the rotational anisotropy measurement. (b) Schematic drawing of the experimental geometry. (c/d) Polar plots of the P-polarized component of the SH intensity of some mono- and multilayer flakes of MoS₂ and corresponding fits (solid lines) from which the individual crystal orientations are extracted.

IV. RESULTS AND DISCUSSION

A. Polarization dependent SHG measurements

Previous rotational anisotropy measurements probing the SH radiation component parallel (perpendicular) to the polarization of the fundamental field revealed the expected $\cos^2 3\theta$ ($\sin^2 3\theta$) dependence^{33–38}. Here, θ denotes the angle between the mirror plane in the crystal structure (i.e. the armchair direction) and the polarization of the probe beam. Rotating the sample then allows direct access to the symmetry of the sample and to the crystal orientation^{33–38}. However, in order to exploit the advantage of SH imaging microscopy probing a larger surface area at once, the sample position is chosen to be fixed and the polarization of the fundamental is rotated. As it is known from literature⁶³ and further derived in the supplementary material, the expected dependence of P- and S-polarized components of the SH intensity on the polarization for normal incidence yield

$$I_P^2(\phi) \propto \cos^2(2\phi + 3\Psi) \quad (1)$$

$$I_S^2(\phi) \propto \sin^2(2\phi + 3\Psi). \quad (2)$$

Here, ϕ denotes the angle of the polarization with respect to the horizontal and Ψ the angle between the armchair direction of the 2D-crystal and the horizontal as sketched in Fig. 3(b).

Thus, instead of the three-fold rotational symmetry, a two-fold rotational symmetry is expected for normal incidence. However, in our case of a small angle of incidence, the two-fold symmetry is broken and one observes two pairs of maxima with different heights, but again the crystal orientation can be evaluated from the data. Please note, that because of the three-fold rotational symmetry of the TMDC monolayers, SHG without phase information does not deduce opposite crystal orientations. Consequently, it only determines domain orientations modulo 60° .

A movie of the polarization dependent SHG microscopy measurements showing the P-polarized SH component ($t_{\text{exposure}} = 60 \text{ s}$) for varying polarization of the fundamental from 0° to 360° in steps of 3° can be found in the supplementary material. Fig. 3 shows the corresponding polar plots of the SH intensity of some MoS_2 (c) mono- and (d) multilayer regions marked in the SHG microscopy image (a). As described above, the crystal orientations Ψ of the three MoS_2 mono- and multilayer flakes are evaluated from the observed phase of the corresponding fits. The crystal orientation can also be extracted for every pixel by an automatized fitting routine which is further described in the supplementary material. The result is illustrated in Fig. 2(c). The crystal orientation for each individual flake including overlapping domains and growth errors like twins can be easily identified. One has to point out that the determination of the crystal orientation or stacking angles by means of SHG originates directly from the symmetry properties of the TMDC layers. Neither a complementary experimental technique nor further modelling is needed for the evaluation. This is in contrast to similar considerations for graphene which is, by the way, not accessible by SHG due to its inversion symmetry. Instead, the stacking of bilayer graphene has been studied systematically for example by the combination of structural and optical experimental techniques like transmission electron microscopy and Raman spectroscopy^{64,65}.

B. Time-resolved SHG measurements

The results of a time-resolved pump-probe SHG experiment on the same surface area as in Fig. 3(a) are shown in Fig. 4. The used pump-wavelength of 600 nm (2.07 eV) was chosen to be slightly above the B-exciton resonance of MoS_2 (2.02 eV)²⁰ for generation of A- and B-excitons to gain access to the full domain of possible decay channels. The observed transients for both MoS_2 monolayers and multilayers show an ultrafast pump-induced decrease of the SH response and a subsequent relaxation on a picosecond timescale. The relaxation dynamics considerably differ between mono- and multilayers. The spatial resolution of SHG imaging microscopy is particularly

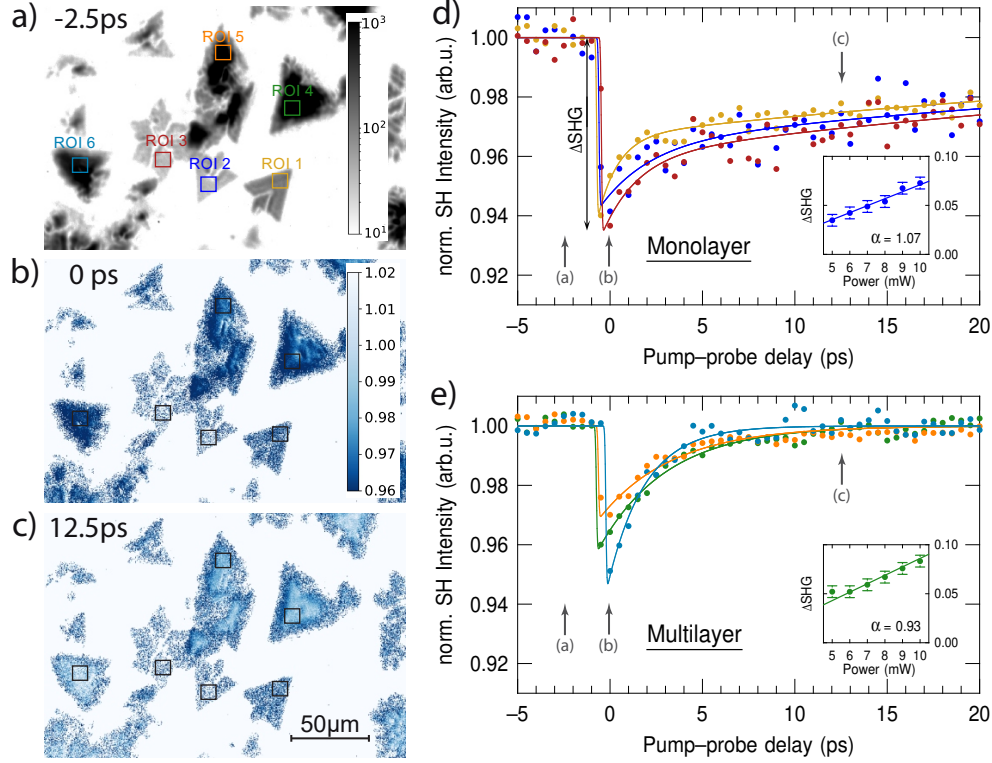


FIG. 4. Time-resolved SHG from MoS₂ monolayer and multilayer flakes upon 600-nm excitation at an applied laser power of 10 mW ($F_{\text{pump}} = 55 \mu\text{J}/\text{cm}^2$). a) SH image of the same area as shown in Fig. 3 at a pump-probe delay of -2.5 ps. b) and c) show normalized SH images at different pump-probe delays of 0 ps and 12.5 ps, respectively. The two images are normalized to an average of ten images at negative delay times, i.e. before excitation. Dark blue color represents a pump-induced decrease in intensity, light blue signifies no change. At temporal overlap (b), a clear decrease of the SH intensity is observed for all MoS₂ flakes. After 12.5 ps (c), the intensity of all flakes has recovered to some extent, in particular in the center of the multilayers flakes. d) and e) show the averaged SH intensities of the individual regions in dependence of the pump-probe delay for monolayers (ROI 1-3) and multilayers (ROI 4-6), respectively. The grey arrows mark the temporal position of the images a), b) and c). The insets show the fluence dependence of the initial decrease of the SH intensity (ΔSHG) as indicated by the arrow in (d).

advantageous to monitor directly the homogeneity of the TMDC monolayers and heterostructures after photoexcitation. As illustrated in Fig. 4(a), the individual monolayer flakes reveal a homogeneous SH response, and the same holds for the transient changes of the monolayers due to photoexcitation. Fig. 4(b) and (c) display SH images at pump-probe delays of 0 ps and 12.5 ps which were normalized to an average of ten images at negative delays. While normalization improves the

visibility of small pump-induced changes, it also amplifies the overall noise level. Thus, the noisy appearance of the monolayer flakes in the normalized images is caused by their lower SH signal and not due to sample degradation. In comparison to the rather homogeneous transient changes of the monolayer flakes, the dynamics of the multilayer flakes exhibit clear inhomogeneity within the flakes such as the apparent differences for the inner and outer part of the multilayer flake at ROI 4. Appropriate regions of interest are therefore chosen to evaluate the transient change for a homogeneous area.

The different monolayer flakes (ROI 1-3, Fig. 4(d)) exhibit very reproducible transients with an initial pump-induced decrease of the SH signal of about 6% followed by a bi-exponential recovery. As determined from a rate-equation model the fast decaying component corresponds to an averaged time-constant of $\tau_1 = 1.9 \pm 0.7$ ps, followed by a second slow component with a time-constant of $\tau_2 = 48.5 \pm 2.1$ ps. In direct comparison, the multilayer flakes (ROI 4-6, Fig. 4(e)) show a slightly larger variance with regard to the initial drop ($\sim 3 - 6\%$) as well as the following dynamics. Most likely, this variance can be attributed to a certain thickness variation of individual multilayer flakes. For all multilayer transients, however, a clear mono-exponential recovery can be observed. The corresponding averaged time-constant is determined to be $\tau = 3.2 \pm 0.9$ ps.

We attribute the fast initial decrease of the SH response to pump-induced changes in the second-order nonlinear susceptibility, e.g., due to the pump-induced depopulation of the valence band associated with the generation of excitons. The subsequent progression is then interpreted as exciton relaxation. Further evidence for this attribution is given by fluence dependent measurements, which exhibit a linear increase of the initial signal change with increasing applied pump power (cf. insets of Fig. 4(d) and (e))⁶⁶. Beside this linear increase, the dynamics of the SH transients do not show any dependence on the applied pump-fluence. Since the latter would have been expected for Auger recombination processes, we attribute the observed lifetimes of the SH signals as defect-mediated non-radiative recombination in accordance with previous reports⁶⁷⁻⁶⁹.

The determined time-constants of the MoS₂ monolayer compare very well with excitonic lifetimes obtained from linear optical spectroscopy^{67,68}. However, the overall number and values of reported time-constants for MoS₂ monolayers differ quite strongly^{18,41,67,68,70-76}. Single-^{41,71,74}, bi-^{18,68,70,72,73,75} and tri-^{67,76} exponential behavior has been reported. The value of the shortest time-constant ranges from 500 fs up to 100 ps and that of the longest time-constant from 15 ps up to 500 ps. For the MoS₂ multilayer, we observe that the overall decay is clearly faster than the monolayer decay. Assuming that the defect densities in the individual layers remain constant

during the CVD growth, our findings could be explained by an enhanced exciton diffusion in the three-dimensional multilayers resulting in a faster trapping compared with the 2D monolayer. Studies comparing directly the dynamics of MoS₂ mono- and multilayers are rare and, furthermore, report contrary effects: While Shi *et al.* report slightly smaller time-constants of few-layer systems⁶⁷, Wang *et al.* found a strong increase of the time-constants with increasing layer number⁶⁹.

Thus, the values and trends in the dynamics of MoS₂ mono- and multilayer systems reported in literature deviate considerably from each other. While the reasons for these differences remain ambiguous, they might be explained especially by varying sample quality and among other things also by the use of different substrates, different temperatures, different pump- and probe energies and laser fluences, and of course, also by systematic effects of the applied techniques. From this lack of clarity for these quite simple 2D mono- and multilayer systems, one might anticipate the complexity for 2D heterostructures and corresponding devices. Thus, systematic time-resolved studies on monolayer and heterostructure systems are mandatory in identifying the genuine physical effects and understanding the underlying mechanisms correlated to the layer stacking. Consequently, this knowledge will facilitate the further development and improvement of prospective applications based on 2D materials.

V. CONCLUSION

We have introduced time-resolved SHG imaging microscopy for the investigation of monolayers and heterostructures of two-dimensional transition metal dichalcogenides. For single- and multilayer MoS₂ flakes grown on SiO₂ / Si(001) crystalline orientations are evaluated from polarization dependent measurements. Time-resolved experiments exhibit an ultrafast pump-induced decrease of the SH response in both systems while their relaxation behavior differs considerably. From the corresponding time-constants the transient changes are attributed to the generation and relaxation of excitons. The results demonstrate that SHG imaging microscopy is a powerful method to investigate the dynamics of charge carriers and excitons of TMDC heterostructure by systematic pump-probe experiments of spatially inhomogeneous samples. The observed transient changes of the second-harmonic response can be readily correlated to the stacking of the material.

ACKNOWLEDGMENTS

Funding by the Deutsche Forschungsgemeinschaft through SFB 1083 is gratefully acknowledged.

DATA AVAILABILITY

Data available on request from the authors.

REFERENCES

- ¹K. S. Novoselov, A. K. Geim, S. V. Morozov, D. Jiang, Y. Zhang, S. V. Dubonos, I. V. Grigorieva, and A. A. Firsov, *Science* **306**, 666 (2004).
- ²K. F. Mak, C. Lee, J. Hone, J. Shan, and T. F. Heinz, *Phys. Rev. Lett.* **105**, 136805 (2010).
- ³A. Splendiani, L. Sun, Y. Zhang, T. Li, J. Kim, C.-Y. Chim, G. Galli, and F. Wang, *Nano Lett.* **10**, 1271 (2010).
- ⁴A. K. Geim and I. V. Grigorieva, *Nature* **499**, 419 (2013).
- ⁵H. Lim, S. I. Yoon, G. Kim, A. R. Jang, and H. S. Shin, *Chem. Mater.* **26**, 4891 (2014).
- ⁶K. F. Mak and J. Shan, *Nat. Photonics* **10**, 216 (2016).
- ⁷D. Xiao, G. B. Liu, W. X. Feng, X. D. Xu, and W. Yao, *Phys. Rev. Lett.* **108**, 196802 (2012).
- ⁸K. F. Mak, K. L. He, J. Shan, and T. F. Heinz, *Nat. Nanotechnol.* **7**, 494 (2012).
- ⁹H. L. Zeng, J. F. Dai, W. Yao, D. Xiao, and X. D. Cui, *Nat. Nanotechnol.* **7**, 490 (2012).
- ¹⁰G. Sallen, L. Bouet, X. Marie, G. Wang, C. R. Zhu, W. P. Han, Y. Lu, P. H. Tan, T. Amand, B. L. Liu, and B. Urbaszek, *Phys. Rev. B* **86**, 081301 (2012).
- ¹¹H. P. Komsa and A. V. Krasheninnikov, *Phys. Rev. B* **88**, 085318 (2013).
- ¹²J. Kang, S. Tongay, J. Zhou, J. B. Li, and J. Q. Wu, *Appl. Phys. Lett.* **102**, 012111 (2013).
- ¹³M. H. Chiu, C. D. Zhang, H. W. Shiu, C. P. Chuu, C. H. Chen, C. Y. S. Chang, C. H. Chen, M. Y. Chou, C. K. Shih, and L. J. Li, *Nat. Commun.* **6**, 7666 (2015).
- ¹⁴V. O. Özcelik, J. G. Azadani, C. Yang, S. J. Koester, and T. Low, *Phys. Rev. B* **94**, 035125 (2016).
- ¹⁵H. M. Hill, A. F. Rigosi, K. T. Rim, G. W. Flynn, and T. F. Heinz, *Nano Lett.* **16**, 4831 (2016).
- ¹⁶C. H. Lee, G. H. Lee, A. M. van der Zande, W. C. Chen, Y. L. Li, M. Y. Han, X. Cui, G. Arefe, C. Nuckolls, T. F. Heinz, J. Guo, J. Hone, and P. Kim, *Nat. Nanotechnol.* **9**, 676 (2014).

- ¹⁷X. P. Hong, J. Kim, S. F. Shi, Y. Zhang, C. H. Jin, Y. H. Sun, S. Tongay, J. Q. Wu, Y. F. Zhang, and F. Wang, *Nat. Nanotechnol.* **9**, 682 (2014).
- ¹⁸F. Ceballos, M. Z. Bellus, H. Y. Chiu, and H. Zhao, *ACS Nano* **8**, 12717 (2014).
- ¹⁹P. Rivera, J. R. Schaibley, A. M. Jones, J. S. Ross, S. F. Wu, G. Aivazian, P. Klement, K. Seyler, G. Clark, N. J. Ghimire, J. Q. Yan, D. G. Mandrus, W. Yao, and X. D. Xu, *Nat. Commun.* **6**, 6242 (2015).
- ²⁰A. F. Rigosi, H. M. Hill, Y. Li, A. Chernikov, and T. F. Heinz, *Nano Lett.* **15**, 5033–38 (2015).
- ²¹D. Kozawa, A. Carvalho, I. Verzhbitskiy, F. Giustiniano, Y. Miyauchi, S. Mouri, A. H. C. Neto, K. Matsuda, and G. Eda, *Nano Lett.* **16**, 4087 (2016).
- ²²H. M. Zhu, J. Wang, Z. Z. Gong, Y. D. Kim, J. Hone, and X. Y. Zhu, *Nano Lett.* **17**, 3591 (2017).
- ²³P. Merkl, F. Mooshammer, P. Steinleitner, A. Girnghuber, K. Q. Lin, P. Nagler, J. Holler, C. Schüller, J. M. Lupton, T. Korn, S. Ovesen, S. Brem, E. Malic, and R. Huber, *Nat. Mater.* **18**, 691 (2019).
- ²⁴K. H. Liu, L. M. Zhang, T. Cao, C. H. Jin, D. A. Qiu, Q. Zhou, A. Zettl, P. D. Yang, S. G. Louie, and F. Wang, *Nat. Commun.* **5**, 4966 (2014).
- ²⁵S. J. Zheng, L. F. Sun, X. H. Zhou, F. C. Liu, Z. Liu, Z. X. Shen, and H. J. Fan, *Adv. Opt. Mater.* **3**, 1600 (2015).
- ²⁶R. Akashi, M. Ochi, S. Bordacs, R. Suzuki, Y. Tokura, Y. Iwasa, and R. Arita, *Phys. Rev. Appl.* **4**, 014002 (2015).
- ²⁷P. C. Yeh, W. Jin, N. Zaki, J. Kunstmann, D. Chenet, G. Arefe, J. T. Sadowski, J. I. Dadap, P. Sutter, J. Hone, and R. M. Osgood, *Nano Lett.* **16**, 953 (2016).
- ²⁸H. Y. Yu, Y. Wang, Q. J. Tong, X. D. Xu, and W. Yao, *Phys. Rev. Lett.* **115**, 187002 (2015).
- ²⁹W. C. Jin, P. C. Yeh, N. Zaki, D. T. Zhang, J. T. Liou, J. T. Sadowski, A. Barinov, M. Yablonskikh, J. I. Dadap, P. Sutter, I. P. Herman, and R. M. Osgood, *Phys. Rev. B* **91**, 121409 (2015).
- ³⁰H. Wang, J. Bang, Y. Y. Sun, L. B. Liang, D. West, V. Meunier, and S. B. Zhang, *Nat. Commun.* **7**, 11504 (2016).
- ³¹H. Heo, J. H. Sung, S. Cha, B. G. Jang, J. Y. Kim, G. Jin, D. Lee, J. H. Ahn, M. J. Lee, J. H. Shim, H. Choi, and M. H. Jo, *Nat. Commun.* **6**, 7372 (2015).
- ³²H. Zeng, G.-B. Liu, J. Dai, Y. Yan, B. Zhu, R. He, L. Xie, S. Xu, X. Chen, W. Yao, and X. Cui, *Sci. Rep.* **3**, 1608 (2013).
- ³³Y. Li, Y. Rao, K. F. Mak, Y. You, S. Wang, C. R. Dean, and T. F. Heinz, *Nano Lett.* **13**, 3329 (2013).

- ³⁴L. M. Malard, T. V. Alencar, A. P. M. Barboza, K. F. Mak, and A. M. de Paula, *Phys. Rev. B* **87**, 201401 (2013).
- ³⁵N. Kumar, S. Najmaei, Q. Cui, F. Ceballos, P. M. Ajayan, J. Lou, and H. Zhao, *Phys. Rev. B* **87**, 161403 (2013).
- ³⁶C. Janisch, Y. X. Wang, D. Ma, N. Mehta, A. L. Elias, N. Perea-Lopez, M. Terrones, V. Crespi, and Z. W. Liu, *Sci. Rep.* **4**, 5530 (2014).
- ³⁷Y. Miyauchi, R. Morishita, M. Tanaka, S. Ohno, G. Mizutani, and T. Suzuki, *Jpn. J. Appl. Phys.* **55**, 085801 (2016).
- ³⁸X.-Q. Zhang, C.-H. Lin, Y.-W. Tseng, K.-H. Huang, and Y.-H. Lee, *Nano Lett.* **15**, 410 (2015).
- ³⁹X. Yin, Z. Ye, D. A. Chenet, Y. Ye, K. O'Brien, J. C. Hone, and X. Zhang, *Science* **344**, 488 (2014).
- ⁴⁰W.-T. Hsu, Z.-A. Zhao, L.-J. Li, C.-H. Chen, M.-H. Chiu, P.-S. Chang, Y.-C. Chou, and W.-H. Chang, *ACS Nano* **8**, 2951 (2014).
- ⁴¹E. M. Mannebach, K.-A. N. Duerloo, L. A. Pellouchoud, M.-J. Sher, S. Nah, Y.-H. Kuo, Y. Yu, A. F. Marshall, L. Cao, E. J. Reed, and A. M. Lindenberg, *ACS Nano* **8**, 10734 (2014).
- ⁴²G. Wang, X. Marie, I. Gerber, T. Amand, D. Lagarde, L. Bouet, M. Vidal, A. Balocchi, and B. Urbaszek, *Phys. Rev. Lett.* **114**, 097403 (2015).
- ⁴³D. W. Li, W. Xiong, L. J. Jiang, Z. Y. Xiao, H. R. Golgir, M. M. Wang, X. Huang, Y. S. Zhou, Z. Lin, J. F. Song, S. Ducharme, L. Jiang, J. F. Silvain, and Y. F. Lu, *ACS Nano* **10**, 3766 (2016).
- ⁴⁴K. Y. Yao, E. Yanev, H. J. Chuang, M. R. Rosenberger, X. Y. Xu, T. Darlington, K. M. McCreary, A. T. Hanbicki, K. Watanabe, T. Taniguchi, B. T. Jonker, X. Y. Zhu, D. N. Basov, J. C. Hone, and P. J. Schuck, *ACS Nano* **14**, 708 (2020).
- ⁴⁵C. V. Shank, R. Yen, and C. Hirlimann, *Phys. Rev. Lett.* **51**, 900 (1983).
- ⁴⁶H. W. K. Tom, G. D. Aumiller, and C. H. Brito-Cruz, *Phys. Rev. Lett.* **60**, 1438 (1988).
- ⁴⁷U. Höfer, *Appl. Phys. A-Mater. Sci. Process.* **63**, 533 (1996).
- ⁴⁸C. Voelkmann, M. Reichelt, T. Meier, S. W. Koch, and U. Höfer, *Phys. Rev. Lett.* **92**, 127405 (2004).
- ⁴⁹M. Mauerer, I. L. Shumay, W. Berthold, and U. Hofer, *Phys. Rev. B* **73**, 245305 (2006).
- ⁵⁰J. A. McGuire, M. B. Raschke, and Y. R. Shen, *Phys. Rev. Lett.* **96**, 087401 (2006).
- ⁵¹J. Qi, M. S. Yeganeh, I. Koltover, A. G. Yodh, and W. M. Theis, *Phys. Rev. Lett.* **71**, 633 (1993).
- ⁵²G. Lupke, *Surf. Sci. Rep.* **35**, 77 (1999).

- ⁵³W. A. Tisdale, K. J. Williams, B. A. Timp, D. J. Norris, E. S. Aydil, and X. Y. Zhu, *Science* **328**, 1543 (2010).
- ⁵⁴G. T. Boyd, Y. R. Shen, and T. W. Hansch, *Opt. Lett.* **11**, 97 (1986).
- ⁵⁵K. A. Schultz and E. G. Seebauer, *J. Chem. Phys.* **97**, 6958 (1992).
- ⁵⁶K. Klass, G. Mette, J. Güdde, M. Dürr, and U. Höfer, *Phys. Rev. B* **83**, 125116 (2011).
- ⁵⁷K. Wu, J. D. Canterbury, P. T. Wilson, and M. C. Downer, *Phys. Status Solidi C* **0**, 3081 (2003).
- ⁵⁸T. Manaka, E. Lim, R. Tamura, and M. Iwamoto, *Nat. Photonics* **1**, 581 (2007).
- ⁵⁹H. Satou, Y. Ohshima, H. Kohn, T. Manaka, and M. Iwamoto, *J. Appl. Phys.* **109**, 054506 (2011).
- ⁶⁰J. D. Morris, T. L. Atallah, C. J. Lombardo, H. Park, A. Dodabalapur, and X. Y. Zhu, *Appl. Phys. Lett.* **102**, 033301 (2013).
- ⁶¹J. Gao, B. C. Li, J. W. Tan, P. Chow, T. M. Lu, and N. Koratkar, *ACS Nano* **10**, 2628 (2016).
- ⁶²S. X. Yang, J. Kang, Q. Yue, and K. Yao, *J. Phys. Chem. C* **118**, 9203 (2014).
- ⁶³T. F. Heinz, M. M. T. Loy, and W. A. Thompson, *Phys. Rev. Lett.* **54**, 63 (1985).
- ⁶⁴K. Kim, S. Coh, L. Z. Tan, W. Regan, J. M. Yuk, E. Chatterjee, M. F. Crommie, M. L. Cohen, S. G. Louie, and A. Zettl, *Phys. Rev. Lett.* **108**, 246103 (2012).
- ⁶⁵R. W. Havener, H. L. Zhuang, L. Brown, R. G. Hennig, and J. Park, *Nano Lett.* **12**, 3162 (2012).
- ⁶⁶Y. M. You, X. X. Zhang, T. C. Berkelbach, M. S. Hybertsen, D. R. Reichman, and T. F. Heinz, *Nat. Phys.* **11**, 477 (2015).
- ⁶⁷H. Shi, R. Yan, S. Bertolazzi, J. Brivio, B. Gao, A. Kis, D. Jena, H. G. Xing, and L. B. Huang, *ACS Nano* **7**, 1072 (2013).
- ⁶⁸H. N. Wang, C. J. Zhang, and F. Rana, *Nano Lett.* **15**, 339 (2015).
- ⁶⁹H. N. Wang, C. J. Zhang, and F. Rana, *Nano Lett.* **15**, 8204 (2015).
- ⁷⁰T. Korn, S. Heydrich, M. Hirmer, J. Schmutzler, and C. Schüller, *Appl. Phys. Lett.* **99**, 102109 (2011).
- ⁷¹R. Wang, B. A. Ruzicka, N. Kumar, M. Z. Bellus, H. Y. Chiu, and H. Zhao, *Phys. Rev. B* **86**, 045406 (2012).
- ⁷²Q. S. Wang, S. F. Ge, X. Li, J. Qiu, Y. X. Ji, J. Feng, and D. Sun, *ACS Nano* **7**, 11087 (2013).
- ⁷³D. Z. Sun, Y. Rao, G. A. Reider, G. G. Chen, Y. M. You, L. Brezin, A. R. Harutyunyan, and T. F. Heinz, *Nano Lett.* **14**, 5625 (2014).
- ⁷⁴M. Seo, H. Yamaguchi, A. D. Mohite, S. Boubanga-Tombet, J. C. Blancon, S. Najmaei, P. M. Ajayan, J. Lou, A. J. Taylor, and R. P. Prasankumar, *Sci. Rep.* **6**, 21601 (2016).

⁷⁵S. Cha, J. H. Sung, S. Sim, J. Park, H. Heo, M. H. Jo, and H. Choi, Nat. Commun. **7**, 10768 (2016).

⁷⁶T. Goswami, R. Rani, K. S. Hazra, and H. N. Ghosh, J. Phys. Chem. Lett. **10**, 3057 (2019).